On nonequilibrium shrinkage of supercritical CO_2 droplets in a water-carrier microflow

On nonequilibrium shrinkage of supercritical CO_2 droplets in a water-carrier microflow

Ning Qin, John Z. Wen, Baixin Chen, and Carolyn L. Ren

Citation: Appl. Phys. Lett. **113**, 033703 (2018); doi: 10.1063/1.5039507
View online: https://doi.org/10.1063/1.5039507
View Table of Contents: http://aip.scitation.org/toc/apl/113/3
Published by the American Institute of Physics

On nonequilibrium shrinkage of supercritical CO_2 droplets in a water-carrier microflow

Ning Qin,[1] John Z. Wen,[1] Baixin Chen,[2] and Carolyn L. Ren[1,a)]
[1]*Department of Mechanical and Mechatronics Engineering, University of Waterloo, Waterloo N2L 3G1, Ontario, Canada*
[2]*School of Engineering and Physical Sciences, Heriot-Watt University, Edinburgh EH14 4AS, United Kingdom*

(Received 8 May 2018; accepted 2 July 2018; published online 17 July 2018)

We report an experimental study on the hydrodynamic shrinkage of supercritical carbon dioxide ($scCO_2$) microdroplets during a nonequilibrium process. After $scCO_2$ microdroplets are generated by water shearing upon a $scCO_2$ flow in a micro T-junction, they are further visualized and characterized at the midpoint and the ending point of a straight rectangular microchannel (width × depth × length: 150 μm × 100 μm × 1.5 mm). The measured decreases in droplet size by 8%–36% indicate and simply quantify the droplet shrinkage which results from the interphase mass transfer between the droplet and the neighboring water. Using a mathematical model, the shrinkage of $scCO_2$ droplets is characterized by solvent-side mass transfer coefficients (k_s: 1.5×10^{-4}–7.5×10^{-4} m/s) and the Sherwood number (Sh: 7–37). In general, k_s here is two orders of magnitude larger than that of hydrostatic liquid CO_2 droplets in water. The magnitude of Sh numbers highlights the stronger effect of local convections than that of diffusion in the interphase mass transfer. Our results, as reported here, have essential implications for $scCO_2$-based chemical extractions and carbon storage in deep geoformations. *Published by AIP Publishing*. https://doi.org/10.1063/1.5039507

Due to its liquid-like density (10 s–100 s kg/m^3), gas-like viscosity (10–100 μPa·S), and intermediate diffusion coefficient (10^{-9}–10^{-7} m^2/s) at moderate conditions, among other properties (e.g., nontoxicity and nonflammability), supercritical CO_2 ($scCO_2$) is deemed one of the green solvents.[1,2] In order to enhance mass transfer as well as reaction rates, processes involving $scCO_2$ have been tested in microfluidics for about a dozen years. Among these attempts, $scCO_2$ has been mostly used in chemical reactions as a solvent[3] or a reactant[4] and in extractions of non-polar compounds or emulsions purely as a solvent.[5–7] Besides, some physical properties of $scCO_2$, e.g., solubility,[8] can be probed in microfluidic devices, analogous to that of gaseous CO_2 which receives much more attention.[9,10] On the other hand, the environmental impact of CO_2 nowadays makes demands for mitigation solutions, e.g., carbon capture and storage in which CO_2 is injected and stored at a supercritical state in deep geoformations. The injected fluid-phase CO_2 is likely to form a partially miscible fluid pair with the resident water within nano- to micro-scale pores and throats resulting a binary mixture region at the interface (i.e., nonzero-thickness boundary) in view of the solubility and diffusivity of CO_2. In this case, an interphase mass transfer occurs mainly driven by dissolution, diffusion, and potential local convection. This mechanism (sometimes simply called "dissolution trapping") of CO_2 storage assists in ensuring a secure carbon storage on a long term. Some experimental studies have reported the shrinkage of CO_2 bubbles or segments in contact with miscellaneous liquids.[11–17] The interphase mass transfer between liquid CO_2 droplets and water as well as a resulted shrinkage has been investigated, suggesting a mass transfer coefficient of 10^{-7}–10^{-6} m/s.[18–20] Nevertheless, there are few studies of the shrinkage of $scCO_2$ droplets in contact with aqueous phases which indeed have essential implications for $scCO_2$ based extractions, reactions, and CO_2 storage.

Due to the chemical potential, shrinkage of $scCO_2$ droplets can be foreseen as an essentially nonequilibrium process during an early stage of their contact.[16] The nonequilibrium nature of the interface mass transfer mainly lies in the fact that the microscopic concentration field of CO_2 in the binary region is time-dependent and susceptible to the surrounding hydrodynamic and/or thermodynamic effects.[21,22] Nevertheless, possible shrinkage of individual $scCO_2$ droplets, based on certain statistics, can be evaluated quantitatively, for example, using mass transfer coefficients.

In this letter, the shrinkage of flowing $scCO_2$ droplets in a water-carrier microflow is reported. $scCO_2$ microdroplets are first generated at a T-junction microchannel with a rectangular cross-section (width × depth: 150 μm × 100 μm) in a silicon-glass microchip[23] (74 mm × 44 mm × 1.2 mm) and then measured in terms of their length (L_x) and speed (v_x) at specified positions (x) along a long straight channel, as shown by Fig. 1. An experimental setup (see Fig. S1 in the supplementary material) for high-pressure microfluidic studies is utilized here to fulfill the experimental study. At the T-junction, pre-conditioned $scCO_2$ is dispersed from the side channel into the straight channel where DI water flows, shears, and squeezes off the CO_2 stream, forming $scCO_2$ microdroplets. Given an appropriate flow rate ratio (Q_{scCO2}/Q_{H2O}) of $scCO_2$ and water, the droplet generation at the T-junction becomes periodical and the size (L_1) of generated droplets is overall constant.[24] By comparing L_x at these three positions, the reduction in droplet length can be obtained. Generally, droplet visualization and measurement at each position are achieved by: (1) using a microscope (BX51,

a)E-mail: c3ren@uwaterloo.ca

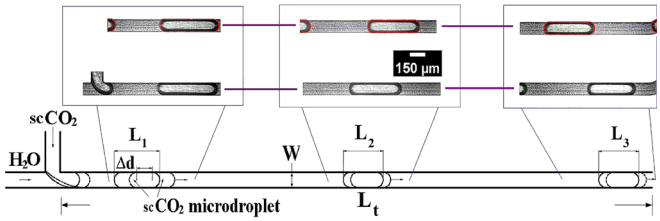

FIG. 1. Schematic of the experimental method. Droplet length L_x and speed v_x are simultaneously measured immediately after droplet generation (position 1), at the midpoint (position 2) and at the end (position 3) of a straight microchannel ($L_t = 15$ mm, $W = 150\ \mu$m), see Sec. S3 in the supplementary material. Δd is a (centroid-to-centroid) drop displacement within one time interval (~1/fps).

Olympus) equipped with a high speed camera (v210, Phantom) working with a rate of 3000 frames per second (fps) and (2) video analyses for L_x and v_x using in-house developed Matlab (R2014a, Mathworks) codes based on identifying droplets and their centroids. For maintaining a supercritical state, CO_2 at its pump, in the facilitating stainless steel tubing (inner diameter: ~570 μm), and at the microchip, is regulated beyond 8 MPa and at 40 °C.

Two groups of Q_{scCO2}/Q_{H2O} are investigated: (1) $10/90 \le Q_{scCO2}/Q_{H2O} \le 75/25$, and $Q_{scCO2} + Q_{H2O} = 100\ \mu$l/min and (2) $50/280 \le Q_{scCO2}/Q_{H2O} \le 50/100$, and $Q_{scCO2} = 50\ \mu$l/min. Note that the minimum and the maximum ratio applied here are a lower and an upper limit rendering observable $scCO_2$ droplet flows at the micro T-junction with an imaging area of $1600\ \mu m \times 400\ \mu m$. The capillary number ($Ca_c = \eta_c v_c/\gamma$) of the continuous phase (i.e., DI water) at the T-junction is calculated, ranging from 1.1×10^{-3} to 1.2×10^{-2}, where the viscosity, $\eta_c = 655.5\ \mu$Pa·s[25] and interfacial tension, $\gamma = 33.5\ mN \cdot m^{-1}$ (Refs. 26–28) are referred to those at a temperature of 313 K and a pressure of 7776–7940 kPa, and the characteristic velocity, v_c, is determined by $v_c = Q_{H2O}/(WD/2)$ by assuming water occupies a half width of the channel on average. The generation of $scCO_2$ droplets is mostly in a squeezing regime in which the interfacial tension dominates over the shear stress. Despite this, a transition to a dripping regime where shear stresses become important is anticipated as the water flow reaches 200 μl/min leading to Ca_c ~0.01.[29] By then, the injected $scCO_2$ stream is unable to touch the channel wall and very small droplets ($L_1/W \le 2$) are produced.

Figures 2(a) and 2(b) provides a collection of snapshots of the representative $scCO_2$ microdroplet at each of the three positions and shows a nondimensionalized size (L_x/W) as well as an overall relative shrinkage of the $scCO_2$ droplet. L_1/W can be linearly correlated to Q_{scCO2}/Q_{H2O} in a T-junction with its geometry known, and $L_1/W = 1 + \alpha \cdot (Q_{scCO2}/Q_{H2O})$ according to Garstecki *et al.*[24] It is found in this study that $\alpha \approx 3.6$ for $Q_{scCO2} + Q_{H2O} = 100\ \mu$l/min ($0.1 < Q_{scCO2}/Q_{H2O} < 2.3$) and $\alpha \approx 2.0$ for $Q_{scCO2} = 50\ \mu$l/min ($0.2 < Q_{scCO2}/Q_{H2O} < 0.5$), respectively, both are greater than 1. In fact, simultaneous squeezing and dragging effects of water over the interface, leading to the pinch-off of the $scCO_2$ stream at the junction, have extended the truncation time for droplets. Thus, it amplifies the contribution of Q_{scCO2} relative to Q_{H2O} in increasing the size of the emerging droplet. Notably, the

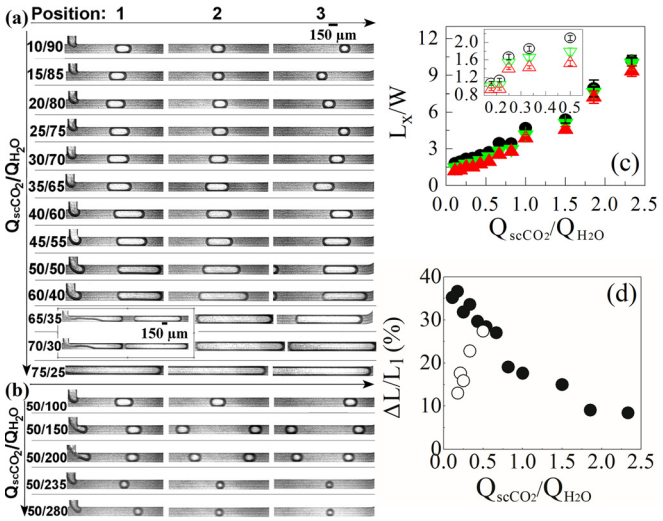

FIG. 2. Overview of $scCO_2$ droplets at three positions for the group (a) $Q_{scCO2} + Q_{H2O} = 100\ \mu$l/min and (b) $Q_{scCO2} = 50\ \mu$l/min. (c) Dimensionless droplet length L_x/W [x = 1 (circles), 2 (down triangles) or 3 (up triangles)]. (d) Overall relative droplet shrinkage $\Delta L/L_1$ ($\Delta L = L_1 - L_3$). In (c) and (d), the solid and open symbols correspond to (a) and (b), respectively.

smaller α for the latter group is due to increased shear effects as Q_{H2O} increases and accelerates the droplet formation. By comparing L_x/W at a specific Q_{scCO2}/Q_{H2O}, a decreasing trend from position 1 to 2 and down to 3 exists, i.e., $L_1/W > L_2/W > L_3/W$, and is applicable to the two groups of Q_{scCO2}/Q_{H2O} [see Fig. 2(c)]. This trend simply indicates the shrinkage of $scCO_2$ microdroplets. The shrinkage is a result of the interphase mass transfer of CO_2 molecules driven by a synergic dissolution-diffusion mechanism due to CO_2 solubility in water and a consequent concentration gradient of CO_2. Besides, local convections near the interface are able to accelerate the mass transfer by continuously refreshing the solvent.[30,31] The overall shrinkage can be divided into two stages, $\Delta L_1 = L_1 - L_2$ and $\Delta L_2 = L_2 - L_3$. It is found that $\Delta L_1 \ge \Delta L_2$ generally applies to the cases of $Q_{scCO2}/Q_{H2O} \le 1$. It means that a rapid shrinkage occurs during the early stage of the droplet flow. Similar behaviors of CO_2 bubbles are reported by Shim *et al.*[16] and an early rapid dissolution regime and a subsequent equilibrium regime are identified. During the early stage, dissolution controls the shrinkage prior to saturation. Later, diffusion and convection start to manifest since saturation is achieved at the near-CO_2 boundary of the binary mixture zone where diffusion is kinetically slower. Thus, shrinkage during later time is less. Besides, ΔL_1 almost equals to ΔL_2 when $Q_{H2O} > 100\ \mu$l/min [see the inset in Fig. 2(c)], implying that dissolution is still dominant given that the residence time of $scCO_2$ droplets in the channel is much shortened. However, a clear distinction of ΔL_1 from ΔL_2 is not observed for $Q_{scCO2}/Q_{H2O} > 1$ [see Fig. 2(c)] due to the deviation of L_x. ΔL of droplets at $Q_{scCO2} + Q_{H2O} = 100\ \mu$l/min are averaged as $(115 \pm 3.4)\ \mu$m, but varies nearly linearly from 86 to 20 μm as Q_{scCO2}/Q_{H2O} tuned from 50/100 to 50/280. The shrinkage may be considered in a relative way in terms of $\Delta L/L_1$ [see Fig. 2(d)]. For the group $Q_{scCO2} + Q_{H2O} = 100\ \mu$l/min, increasing Q_{scCO2}/Q_{H2O} leads to decreasing $\Delta L/L_1$ from 35% to <10% almost linearly. However, the interrelation is reverse for $Q_{scCO2} = 50\ \mu$l/min. These reveal ΔL is closely

related to the flowing time of droplets in the channel that can be quantified using droplet speeds.

Analogous to L_x, the droplet speed v_x ($x = 1$, 2, or 3) is measured at all three positions and presented in Fig. S3 in the supplementary material. For the group $Q_{scCO2} + Q_{H2O} = 100\,\mu$l/min, v_x is ~100 mm/s at various Q_{scCO2}/Q_{H2O} despite variations at the three positions and different variation behaviors at different Q_{scCO2}/Q_{H2O} (relevant discussions are provided in the supplementary material). For the group $Q_{scCO2} = 50\,\mu$l/min, v_x increases linearly from ~120 to ~360 mm/s on average as Q_{scCO2}/Q_{H2O} is tuned from 50/100 to 50/280. When v_x reaches 300 mm/s at $Q_{scCO2}/Q_{H2O} < 50/200$, the flowing time ($t_f$, ms) of droplets becomes very short (~50 ms) leading to very subtle droplet shrinkage [see the inset in Fig. 2(c)]. In order to evaluate the flowing time, v_x are averaged to a characteristic droplet speed ($\bar{v}$) for each flow case. $\bar{v}$ and t_f are calculated [$\bar{v} = (\sum_{x=1}^{3} v_x)/3$ and $t_f = L_t'/\bar{v}$] and shown in Fig. S4. By using L_x and t_f, the solvent-side mass transfer coefficient k_s that characterizes the hydrodynamic shrinkage of $scCO_2$ droplets can be determined. Starting from a differential form of k_s [$k_s = \frac{C_d}{C_e}\frac{d(V)}{Adt}$] in an infinitesimal time step, we obtained a specific form of k_s (see detailed derivations in Sec. S5 in the supplementary material) by accounting for a typical Taylor droplet in a rectangular microchannel at a 3D scenario and based on rewriting the surface area (A, m^2) and volume (V, m^3) of the droplet in terms of the readily available parameters (e.g., W, D, and L_x), as follows:

$$k_s(\text{mm/s}) = \frac{(0.96WD - 0.0632W^2)}{(1.548W + 2D)}\frac{C_d}{C_e}\left(ln\frac{A_0}{A_x}\right)\frac{1}{t}, \quad (1)$$

where C_d and C_e are nominal "molar concentrations" ($C_d = \rho_{scCO2}/M$, mol/L) of CO_2 and its solubility in water, respectively. The term $\Delta C = C_e - C_0$ (the surrounding CO_2 concentration $C_0 \sim 0$) refers to the driving concentration difference for the water-side mass transfer. For calculating A, the contact angle [$\theta_c = (141 \pm 1.2)°$] between the droplet and water at the channel wall averaged from all imaging frames is applied. In order to calculate k_s, C_d is determined by ρ_{scCO2} and the molar mass M, and C_e [(1.153 ± 0.005) mol/l] is referred to that at 313 K and a pressure of 8185–8284 kPa.[32,33]

k_s are calculated by L_1, L_3, and t_f and shown in Fig. 3(a). Note that $k_{s,1-3}$ here is a convective mass transport coefficient[34] accounting for the hydrodynamics within both the droplet and the water slug, as well as in the vicinity of the droplet meniscus. Based on the CO_2 diffusivity ($D_{dc} \approx 1.5 \times 10^{-9}$ m^2/s)[35] in water at the experimental condition and a half channel width as a characteristic length ($L_{mass} = W/2$) for the mass transfer, the Sherwood number [$Sh = k_{s,1-3}/(D_{dc}/L_{mass})$] that compares the strength of the convective mass transfer with that of diffusion can be determined, as shown in Fig. 3(b).

To assist with discussions, we performed a simple CFD study of a single flowing (100 mm/s) $scCO_2$ droplet with water in the long straight microchannel as the computational domain. A VOF (volume-of-fluid) method based on a fraction function of the two phases is adopted in CFD software Fluent (version 17, Ansys, Inc.). In addition, an overall continuity and a momentum equation, as well as a continuum surface (force) tension model and the contact angle (θ_c) are applied. The fluid properties (density and viscosity of water and that as well as diffusivity of $scCO_2$) are considered by referring to the aforementioned pressures and temperature. Flow streamlines (after subtracting a superficial velocity of 100 mm/s from the domain) within the droplet and water corresponding to the moment when the droplet arrives at position 2 [see Figs. 3(d)–3(f)] reveal that toroidal vortexes are formed within the droplet and the water region close to the droplet meniscus. The convective hydrodynamics near the droplet meniscus dominate in transporting CO_2 by continuously refreshing the meniscus region and bringing away dissolved CO_2.

As shown in Figs. 3(a) and 3(b), a negative logarithmic relation is found for both $k_{s,1-3}$ and the Sh number with Q_{scCO2}/Q_{H2O}. Same relations between these two parameters and L_x/W may exist as well in view of a linear correlation of Q_{scCO2}/Q_{H2O} and L_x/W. For a small $scCO_2$ droplet (i.e., small L_1/W), it presents better mass transfer (higher k_s) and

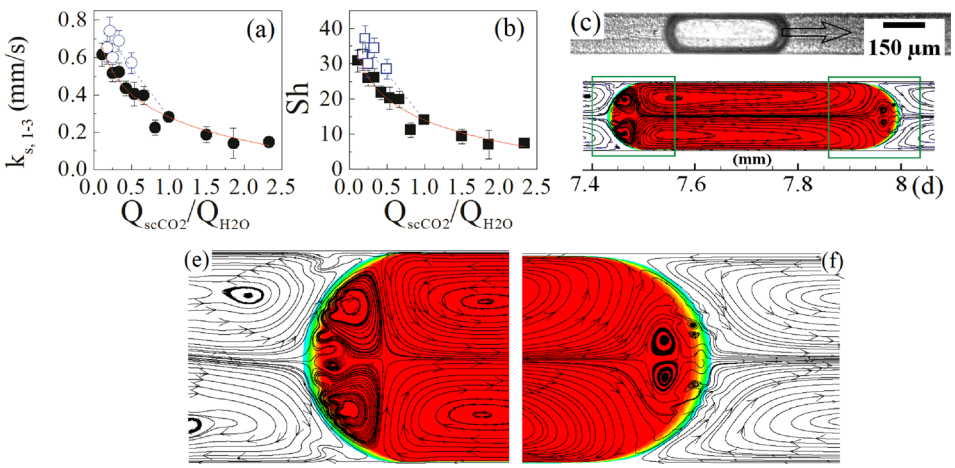

FIG. 3. (a) Mass transfer coefficient $k_{s,1-3}$ and (b) Sherwood numbers. In (a) and (b), solid symbols: $Q_{scCO2} + Q_{H2O} = 100\,\mu$l/min; hollow symbols: $Q_{scCO2} = 50\,\mu$l/min. The error bar indicates one standard deviation according to error propagation. The fitting lines are added for discussions only. (c) A snapshot of a flowing (~100 mm/s, from left to right) $scCO_2$ droplet at position 2 in the channel. (d) Numerically computed flow streamlines within the flowing droplet (red colored) and water slugs (white regions) near the meniscus. Local convections represented by vortexes are detailed in magnified views in (e) and (f). For reference, the magnitude of water velocity near the droplet meniscus is ~30 mm/s.

enhanced dominance of convection over diffusion in controlling the mass transport of CO_2 (larger *Sh*). This disparity is highlighted as well for the same Q_{scCO2}/Q_{H2O} but with an increased Ca_c that results in even smaller CO_2 droplets. Generally, small droplets feature a larger effective portion of an overall interfacial region for the mass transfer and this convection-featured portion contributes more in the mass transport. Moreover, as droplets have a comparably small size, increased Ca_c indicating enhanced shear effects relative to interfacial tension strengthens the convection in the vicinity of the droplet meniscus that promotes the mass transport further.

In conclusion, we have experimentally reported on the shrinkage of flowing $scCO_2$ microdroplets in a water-carrier flow in a straight microchannel. Using a micro T-junction, $scCO_2$ droplets (surface-to-volume ratios $\sim 33.2\,mm^{-1}$) are produced by applying a series of Q_{scCO2}/Q_{H2O} and their length, speed, and the flowing time are either measured or calculated. A mathematical model of the solvent-side mass transfer coefficient (k_s) is developed by accounting for the 3D morphology of a typical Taylor droplet in a rectangular microchannel. k_s in our work ranges from 1.5×10^{-4} to 7.5×10^{-4} m/s which is two orders of magnitude higher than that of the hydrostatic liquid CO_2 droplets in water.[18–20] The *Sh* (7–37) number reveals the dominance of convections over diffusion in controlling the mass transfer. These findings highlight the benefits of using $scCO_2$ and small droplets in a hydrodynamic scenario when it comes to applications of CO_2 in chemical processes and deep underground or oceanic CO_2 storage.

See supplementary material for a schematic of the experimental setup, measurements of droplet length and speed, and a detailed development of the mathematical model of the solvent-side mass transfer coefficient.

We thank Yuk Hei Wong for the Matlab codes for droplet measurements and acknowledge the financial support from the Carbon Management Canada (Theme C: Secure Carbon Storage, Project C393).

[1]W. Leitner, Acc. Chem. Res. **35**, 746 (2002).
[2]E. J. Beckman, J. Supercrit. Fluids **28**, 121 (2004).
[3]J. Kobayashi, Y. Mori, and S. Kobayashi, Chem. Commun. **0**, 2567 (2005).
[4]F. Benito-Lopez, R. M. Tiggelaar, K. Salbut, J. Huskens, R. J. Egberink, D. N. Reinhoudt, H. J. Gardeniers, and W. Verboom, Lab Chip **7**, 1345 (2007).
[5]J. A. Lubguban, J. Sun, T. Rajagopalan, B. Lahlouh, S. L. Simon, and S. Gangopadhyay, Appl. Phys. Lett. **81**, 4407 (2002).
[6]T. Rajagopalan, B. Lahlouh, J. A. Lubguban, N. Biswas, S. Gangopadhyay, J. Sun, D. H. Huang, S. L. Simon, A. Mallikarjunan, H. C. Kim, W. Volksen, M. F. Toney, E. Huang, P. M. Rice, E. Delenia, and R. D. Miller, Appl. Phys. Lett. **82**, 4328 (2003).
[7]S. K. Luther and A. Braeuer, J. Supercrit. Fluids **65**, 78 (2012).
[8]N. Liu, C. Aymonier, C. Lecoutre, Y. Garrabos, and S. Marre, Chem. Phys. Lett. **551**, 139 (2012).
[9]H. Fadaei, B. Scarff, and D. Sinton, Energy Fuels **25**, 4829 (2011).
[10]A. Sell, H. Fadaei, M. Kim, and D. Sinton, Environ. Sci. Technol. **47**, 71 (2013).
[11]R. P. Sun and T. Cubaud, Lab Chip **11**, 2924 (2011).
[12]T. Cubaud, M. Sauzade, and R. P. Sun, Biomicrofluidics **6**, 022002 (2012).
[13]E. Tumarkin, Z. H. Nie, J. I. Park, M. Abolhasani, J. Greener, B. Sherwood-Lollar, A. Gunther, and E. Kumacheva, Lab Chip **11**, 3545 (2011).
[14]M. Abolhasani, M. Singh, E. Kumacheva, and A. Gunther, Lab Chip **12**, 1611 (2012).
[15]S. G. R. Lefortier, P. J. Hamersma, A. Bardow, and M. T. Kreutzer, Lab Chip **12**, 3387 (2012).
[16]S. Shim, J. D. Wan, S. Hilgenfeldt, P. D. Panchal, and H. A. Stone, Lab Chip **14**, 2428 (2014).
[17]C. Y. Zhu, C. F. Li, X. Q. Gao, Y. G. Ma, and D. Z. Liu, Int. J. Heat Mass Transfer **73**, 492 (2014).
[18]Y. Fujioka, K. Takeuchi, Y. Shindo, and H. Komiyama, Int. J. Energy Res. **18**, 765 (1994).
[19]H. Teng and A. Yamasaki, Int. J. Heat Mass Transfer **41**, 4315 (1998).
[20]K. Ogasawara, A. Yamasaki, and H. Teng, Energy Fuels **15**, 147 (2001).
[21]S. E. Powers, C. O. Loureiro, L. M. Abriola, and W. J. Weber, Water Resour. Res. **27**, 463, https://doi.org/10.1029/91WR00074 (1991).
[22]T. Zhu and W. Ye, Phys. Rev. E **82**, 036308 (2010).
[23]N. Qin, J. Z. Wen, and C. L. Ren, Phys. Rev. E **95**, 043110 (2017).
[24]P. Garstecki, M. J. Fuerstman, H. A. Stone, and G. M. Whitesides, Lab Chip **6**, 437 (2006).
[25]D. R. Lide, *CRC Handbook of Chemistry and Physics* (CRC Press, Boca Raton, 2005).
[26]F. Tewes and F. Boury, J. Phys. Chem. B **109**, 3990 (2005).
[27]A. Hebach, A. Oberhof, N. Dahmen, A. Kogel, H. Ederer, and E. Dinjus, J. Chem. Eng. Data **47**, 1540 (2002).
[28]A. Georgiadis, G. Maitland, J. P. M. Trusler, and A. Bismarck, J. Chem. Eng. Data **55**, 4168 (2010).
[29]M. De Menech, P. Garstecki, F. Jousse, and H. A. Stone, J. Fluid Mech. **595**, 141 (2008).
[30]A. Gunther, S. A. Khan, M. Thalmann, F. Trachsel, and K. F. Jensen, Lab Chip **4**, 278 (2004).
[31]H. Kinoshita, S. Kaneda, T. Fujii, and M. Oshima, Lab Chip **7**, 338 (2007).
[32]N. Spycher, K. Pruess, and J. Ennis-King, Geochim. Cosmochim. Acta **67**, 3015 (2003).
[33]L. W. Diamond and N. N. Akinfiev, Fluid Phase Equilib. **208**, 265 (2003).
[34]J. R. Welty, C. E. Wicks, G. Rorrer, and R. E. Wilson, *Fundamentals of Momentum, Heat, and Mass Transfer* (John Wiley & Sons, New York, 2009).
[35]N. Qin, J. Z. Wen, and C. L. Ren, Phys. Rev. E **95**, 043111 (2017).